Wednesday 25 Nov

Advances in Cryogenic Electron Microscopy for Quantum and Energy Materials

Free webinar
17.30-18.30 CET | 11.30-12.30 EST

Register here

Lena F. Kourkoutis,
Associate Professor,
Cornell University

Wiley Analytical Science

ThermoFisher SCIENTIFIC

ADVANCED MATERIALS
www.advmat.de

Revealing Electrical-Poling-Induced Polarization Potential in Hybrid Perovskite Photodetectors

Chuntao Lan, Haiyang Zou, Longfei Wang, Meng Zhang, Shuang Pan, Ying Ma, Yiping Qiu, Zhong Lin Wang, and Zhiqun Lin**

Despite recent rapid advances in metal halide perovskites for use in optoelectronics, the fundamental understanding of the electrical-poling-induced ion migration, accounting for many unusual attributes and thus performance in perovskite-based devices, remain comparatively elusive. Herein, the electrical-poling-promoted polarization potential is reported for rendering hybrid organic–inorganic perovskite photodetectors with high photocurrent and fast response time, displaying a tenfold enhancement in the photocurrent and a twofold decrease in the response time after an external electric field poling. First, a robust meniscus-assisted solution-printing strategy is employed to facilitate the oriented perovskite crystals over a large area. Subsequently, the electrical poling invokes the ion migration within perovskite crystals, thus inducing a polarization potential, as substantiated by the surface potential change assessed by Kelvin probe force microscopy. Such electrical-poling-induced polarization potential is responsible for the markedly enhanced photocurrent and largely shortened response time. This work presents new insights into the electrical-poling-triggered ion migration and, in turn, polarization potential as well as into the implication of the latter for optoelectronic devices with greater performance. As such, the utilization of ion-migration-produced polarization potential may represent an important endeavor toward a wide range of high-performance perovskite-based photodetectors, solar cells, transistors, scintillators, etc.

The past decade has witnessed unprecedented progress in metal halide perovskites with a general formula of ABX_3 (A = $CH_3NH_3^+$ (MA), $CH(NH_2)_2^+$ (FA), or Cs; B^{2+} = Pb^{2+} or Sn^{2+}; and X = Cl^-, Br^-, or I^-) for an array of applications,[1–3] including solar cells,[4–6] light-emitting diodes,[7,8] transistors,[9] and photodetectors.[10,11] This emerging class of materials carries a set of intriguing optoelectronic properties such as high optical absorption coefficient, long carrier diffusion length, and excellent carrier mobility.[12,13] Notably, in spite of remarkable attributes noted above, metal halide perovskites are plagued by their high ionic conduction because of the relatively loosely bonded crystal structures,[14] thereby leading to ion migration in the perovskite layer when the corresponding devices are under an external electric field.[15,16] Such an ion-migration issue has been widely recognized as the primary basis for some unusual behaviors in perovskite-based devices (e.g., photocurrent hysteresis,[17] photoinduced phase separation,[18] and the absence of room-temperature transistor behavior),[19] thus resulting in unstable and weakened device performance. Clearly, an in-depth understanding of ion migration in perovskite devices is of key significance. Moreover, the ability to rationally utilize the ion migration may, conversely, open up the possibility of acquiring stable perovskite devices with improved efficiency.

Notably, the electrical-poling process, which induces the ion migration within perovskites via applying an external electric field, has been conducted on hybrid perovskite-based devices for investigating the ion-migration behavior.[20,21] It is also notable that the electrical poling has been centered primarily on perovskite solar cells, demonstrating the effectiveness in improving their power conversion efficiency,[22–24] representing much larger open-circuit voltage[25] and suppressed photocurrent hysteresis.[26] Nevertheless, a majority of current studies applied high voltage (0.2–7.0 V μm^{-1}) for poling to trigger the ion migration.[23,25,26] To date, there has been relatively few research centered on the use of low voltage for poling, which may be due likely to some special structural and morphological requirements for perovskites in order to induce the ion migration at low voltage. Clearly, it is of key importance to use low voltage to reduce the degradation of perovskites during poling when performing detailed study on the poling effect. In addition, despite both solar cells and photodetectors converting light into electricity, perovskite solar cells generally involve the implementation of electron transport layer and hole transport layer; thus, the photoexcited

Dr. C. Lan, Dr. H. Zou, Dr. L. Wang, Dr. M. Zhang, Dr. S. Pan, Prof. Z. L. Wang, Prof. Z. Lin
School of Materials Science and Engineering
Georgia Institute of Technology
Atlanta, GA 30332, USA
E-mail: zhong.wang@mse.gatech.edu; zhiqun.lin@mse.gatech.edu
Dr. C. Lan, Prof. Y. Ma, Prof. Y. Qiu
Key Laboratory of Textile Science & Technology of Ministry of Education
College of Textiles
Donghua University
Shanghai 201620, China
The ORCID identification number(s) for the author(s) of this article can be found under https://doi.org/10.1002/adma.202005481.

DOI: 10.1002/adma.202005481

carriers flow in a predetermined direction. In contrast, for the photodetectors operated under an external electrical field, the current direction can be easily altered by modulating the operating voltage. On the other hand, the investigation into the effects of electrical field with two different directions (i.e., poling and measuring electric field directions) on the transport of electrons and holes is comparatively few and limited in scope. Thus, it is highly desirable to expand the application of electrical poling in other forms of optoelectronic devices for enabling a thorough understanding of the fundamental mechanism of ion migration. The photodetectors can be constructed by using perovskites of different morphologies, such as polycrystalline films, bulk single crystals, nanoplates, and nanowires,[27] thereby conferring the possibility of further exploring the mechanism of electrical-poling-induced ion migration in perovskite materials and consequently exploit it for engineering photodetectors with enhanced performance.

Herein, we report the judicious implementation of small external electrical poling to induce the polarization potential for imparting hybrid organic–inorganic perovskite photodetectors with high photocurrent, responsivity, and fast response time. A meniscus-assisted solution-printing (MASP) strategy is capitalized on to craft hybrid perovskites (i.e., $MAPbBr_3$) into aligned crystals with large grain size and reduced grain boundary. The choice of $MAPbBr_3$ is motivated by its effective optical absorption and relative stability under ambient conditions as compared to the I-containing counterpart ($MAPbI_3$). Prior to the measurement, an external low voltage bias (4 V, an equivalent electric field strength of 0.004 V μm^{-1}) is introduced to pole the perovskite photodetector assembled by using MASP-enabled, oriented $MAPbBr_3$ crystalline layer. The electrical poling yields a tenfold increase in photocurrent (I_{light}) and a twofold decrease in response time (τ) in the crystal-orientation-aligned perovskite photodetectors. Notably, the Kelvin probe force microscopy (KPFM) studies reveal the creation of polarization potential due to the electrical-poling-induced ion migration under the applied voltage. Importantly, this polarization potential effectively modulates the junction barrier, thereby enhancing the collection of photocarriers and thus accounting for the tunable I_{light} of the $MAPbBr_3$-film-based photodetector after poling. Moreover, the effectiveness of electrical poling on the performance of photodetectors is found to be dictated by the forms of the perovskite layer (e.g., film vs stripes). Our study brings fundamental and practical insights into the poling effect on tailoring the optoelectronic properties and highlights the significance of electrical-poling-promoted ion migration and polarization potential in sequence in the perovskite layer for the development of a set of optoelectronic devices with markedly improved performance.

The MASP strategy was employed to produce the $MAPbBr_3$ films with oriented crystals over a large area (see the "Experimental Section"), facilitating the subsequent engineering of $MAPbBr_3$-based photodetectors and their investigation into the electrical-poling effect on the device performance. Nonetheless, **Figure 1**a,b describes the crafting of a layer of $MAPbBr_3$ film by MASP. As illustrated in Figure 1a, a drop of the $MAPbBr_3$ precursor solution (i.e., MABr:$PbBr_2$ at 1:1 molar ratio dissolved in *N*,*N*-dimethylformamide (DMF)) is loaded and confined between the two nearly parallel plates due to the capillary action, where the upper plate (blade) is stationary while the lower plate (substrate) is movable as it is mounted on a computer-controlled translational stage. A concave meniscus is thus formed at the edge of this two nearly parallel plates' geometry with a separation distance between the two plates of 200 μm. A continuous perovskite film over the entire lower substrate is yielded by programmably moving the translational stage where the substrate is placed. It is notable that the meniscus is receded in the direction opposed to the moving direction of the lower substrate, and thus the perovskite film is grown along the meniscus receding direction, as indicated by a black arrow in Figure 1a. Figure 1b displays a cross-sectional view of the meniscus where the nucleation and crystal growth of $MAPbBr_3$ film during the MASP process are depicted.

Upon the solvent evaporation of the precursor DMF solution caused by the heating of the lower substrate at 100 °C, the faster evaporation rate of DMF at the edge of meniscus (i.e., at the lower substrate/perovskite precursor DMF solution/air three-phase contact line) induces an outward convective flow to replenish the evaporative loss of solvent and concurrently transport the solute (i.e., perovskite precursors) to the contact line. Thus, a supersaturated phase of the precursor solution is reached at the contact line because of the continuous accumulation of solutes. Subsequently, the nucleation of $MAPbBr_3$ occurs at the contact line, followed by the crystal growth.[28] Notably, the nucleation and growth process keeps going owing to the sustained replenishing of solute to the growth front (i.e., the contact line), driven by the convective flow as noted above. As a result, a continuous layer of $MAPbBr_3$ film along the moving direction of the lower substrate is yielded after the receding meniscus being progressively swept across the entire substrate.

It is crucial to study the poling effect on perovskite crystals with different morphologies to further explore the mechanism of electrical-poling-induced ion migration in perovskite materials. The MASP strategy enables convenient tailoring of the morphology of the perovskite layer via tuning the concentration of the perovskite precursor solution, the moving speed of the lower plate, and the heating temperature of the lower plate (i.e., the annealing temperature of perovskites). Figure S1a (Supporting Information) depicts the formation of a continuous film and an array of parallel stripes of $MAPbBr_3$ crystals at different precursor concentrations (a cross-sectional view of the meniscus, that is, in the direction perpendicular to the moving substrate) near the contact line. During the nucleation and growth of $MAPbBr_3$, a thin and continuous wet film near the contact line is dried in a short period of time (left panel in Figure S1a in the Supporting Information). At high precursor concentration (c = 50 mg mL^{-1}; upper right panel in Figure S1a in the Supporting Information), sufficient precursors are available at the contact line for crystal growth during the film solidification. Thus, adjacent perovskite crystals connect with each other in the direction perpendicular to the moving substrate within a short time, as indicated in the areas with a dashed box in Figure S1b (Supporting Information). As a result, a continuous $MAPbBr_3$ film over a large surface area is yielded, as revealed by scanning electron microscopy (SEM; Figure 1c,d). As displayed in Figure 1c, the $MAPbBr_3$ crystals within the film were oriented in the direction nearly perpendicular to the film

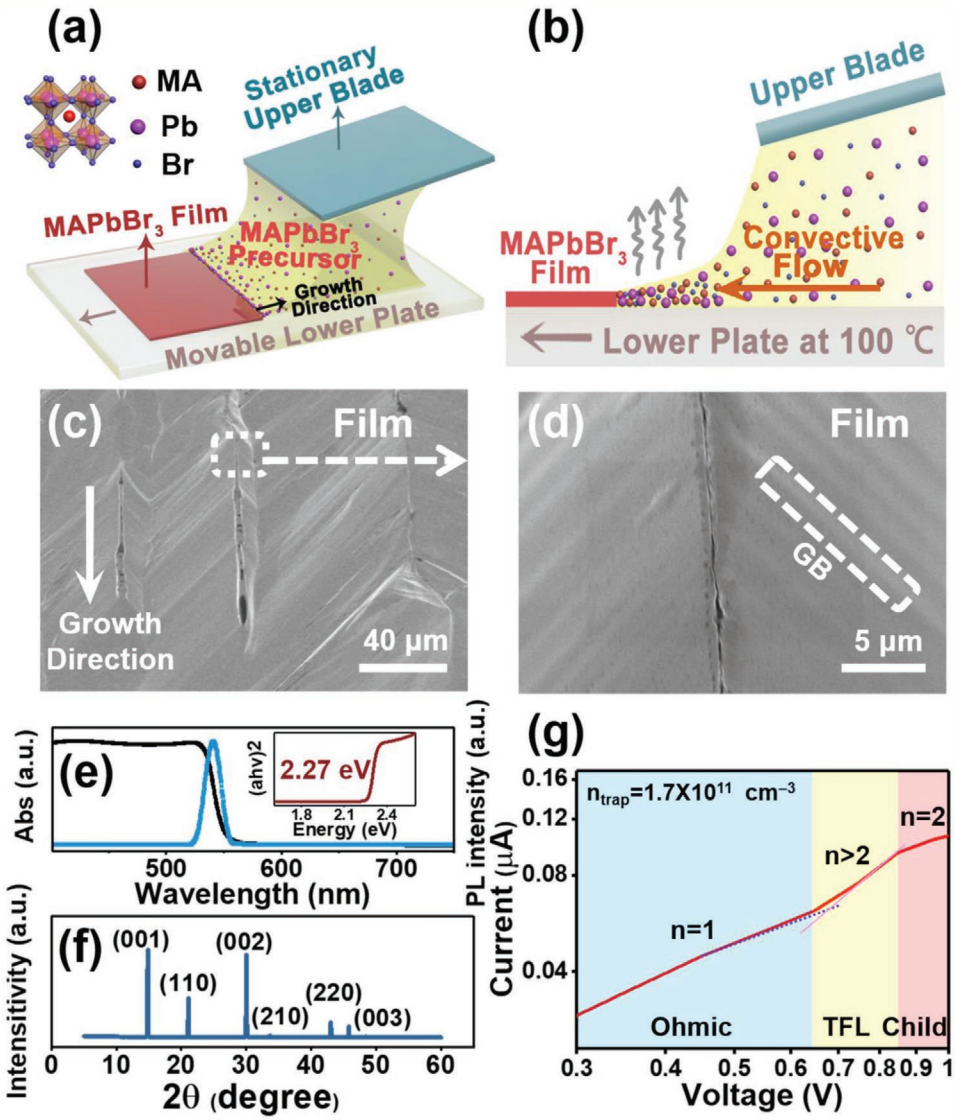

Figure 1. Meniscus-assisted solution printing (MASP) of $MAPbBr_3$ layer. a) Schematic illustration of the 3D view of the MASP process for crafting the $MAPbBr_3$ film. b) A side view of the MASP process, where the meniscus at the edge of two nearly parallel plates is clearly evident. The outward convective flow carries the precursors to the edge of the meniscus, forming an $MAPbBr_3$ film, while the lower flat substrate is heated at 100 °C and moved at a constant velocity against the upper slightly tilted yet stationary blade. c) Low-resolution and d) high-resolution SEM images of the $MAPbBr_3$ film crafted by MASP at the precursor DMF concentration $c = 50$ mg mL^{-1}. The dashed rectangle marks a grain boundary (GB) in $MAPbBr_3$ film. e) Steady-state UV–vis absorption and photoluminescence spectra of the $MAPbBr_3$ film. The inset shows the Tauc plot calculated from the absorption spectrum. f) XRD pattern of the $MAPbBr_3$ film. g) Current–voltage curve of the $MAPbBr_3$ film for space-charge-limited current (SCLC) analysis.

growth direction (as indicated by the white arrow). This is due to the MASP process that guides the convective flow of solutes and controls the crystallization of the $MAPbBr_3$ film.[1,29] The $MAPbBr_3$ film possesses large crystals and nearly invisible small gaps (i.e., grain boundaries, GBs) between crystal grains (Figure 1d). By contrast, for the low precursor concentration (c = 10 mg mL^{-1}; lower right panel in Figure S1a in the Supporting Information), it is not surprising that the inadequate solutes at the contact line result in separate crystals during their solidification (Figure S1c, Supporting Information), producing separated stripes by MASP, as shown in Figure S2a,b (Supporting Information). The stripes are composed of well-oriented $MAPbBr_3$ crystals along the moving direction of the lower substrate while separating from one another laterally, where the GBs in stripes (Figure S2b, Supporting Information) are much obvious compared to those in $MAPbBr_3$ film (Figure 1d). It is notable that, in contrast to the uniformly distributed crystals in the spin-coating film, the MASP method yielded well-aligned crystals in both $MAPbBr_3$ film and stripes due to the meniscus effect during the nucleation and growth process.[1] In addition, compared to the doctor-blade coating where the solvent evaporation is driven by applying high temperature, the MASP technique promotes the perovskite crystallization by accelerating the solvent evaporation through the meniscus effect, leading to control over the crystal morphology and crystallinity of the perovskite layer.[1]

Owing to the unique crystal formation strategy, the as-obtained $MAPbBr_3$ film possessed high crystallinity and low trap density, as corroborated by steady-state UV–vis and photoluminescence (PL) and X-ray diffraction (XRD) measurements. As shown in Figure 1e, the absorbance of $MAPbBr_3$ film starts from ≈550 nm with a clear band edge cutoff, suggesting high-quality crystals with low defect density in the film. Accordingly, the energy bandgap (E_g) of the film was calculated to be 2.27 eV by extrapolating the linear region of the Tauc plot to a zero level, which is smaller than the reported value of $MAPbBr_3$ film (≈2.30 eV).[30] The PL peak is sharp and located at ≈540 nm. The narrow PL peak signifies a low trap density of the $MAPbBr_3$ film.[31] Figure 1f shows the XRD pattern of the as-prepared $MAPbBr_3$ film. It can be indexed to the cubic perovskite crystal structure, which is in good agreement with that reported in literature.[32] Furthermore, the charge trap density (n_{trap}) of the $MAPbBr_3$ film was calculated according to the space charge limited current (SCLC) theory. By fitting the current–voltage (I–V) curve obtained under the dark, a linear Ohmic region followed by a trap-filled region was obtained, from which the trap-filled limit (TFL) voltage (V_{TFL}) was found to be 0.68 V (Figure 1g). According to the equation $n_{trap} = \frac{2\varepsilon\varepsilon_0 V_{TFL}}{eL^2}$, where ε is the dielectric constant, ε_0 is the vacuum permittivity, e is the elemental charge, and L is the length between to electrodes, the n_{trap} of the MASP $MAPbBr_3$ film was calculated to be 1.7×10^{11} cm^{-3}, comparable to that of the $MAPbBr_3$ single crystals, revealing the low charge traps of the MASP $MAPbBr_3$ film.[33]

Subsequently, the perovskite film crafted by MASP was employed in a photodetector, displaying good photoresponse. The scheme of device architecture as well as the photoresponse measurement is illustrated in **Figure 2**a. The laterally structured photodetector was designed where two silver (Ag) electrodes are bridged by a layer of continuous $MAPbBr_3$ film. The electrodes are perpendicular to the growth direction of the perovskite film during the MASP process (as indicated by the arrow). The distance between the two electrodes was set to be 1 mm. For the photodetector, an applied electric field is usually employed to enhance the photocurrent. In this context, the direction of the external electric field can be altered by applying either a positive or a negative bias voltage, and the direction of the generated photocurrent depends on the applied electric field. Prior to conducting the poling process, the photocurrents under different light intensities were investigated, as shown in Figure S3a (Supporting Information). In typical I–V curves of the device under the various intensities of 442 nm light irradiation (from 0.08 to 27.1 mW cm^{-2}), it is clear that the photocurrent greatly enhanced with the increase of light intensity due to the increment of photoexcited carriers at the elevated light intensity. Notably, the photocurrents generated by positive applied bias voltages (e.g., 18.9 μA at 2 V) were larger than those by the corresponding negative applied bias voltages (e.g., –7.6 μA at –2 V) when measuring under 442 nm visible light illumination at a power density of 27.1 mW cm^{-2}. In addition, the dark current of the device is also asymmetric (e.g., 2.2 μA at 2 V and –1.7 μA at –2 V; Figure S3b, Supporting Information). These I–V curves show a Schottky junction behavior because the generated carriers in the photodetector may have preferential directionality to transport despite the symmetric structure of the device due to the asymmetric morphology of the perovskite film (i.e., the growth direction, crystalline shape, etc., as shown in Figure 1c,d). Moreover, the photocurrent displayed a good linear relationship with the incident light intensity (Figure S3c, Supporting Information) without the photodiode saturation at an intensity of 27.1 mW cm^{-2}, as a silicon-based commercial photodetector usually has a saturation at a relatively high intensity of light (i.e., ≈2 mW cm^{-2}).[34]

Intrigued by the oriented crystals and high crystallinity, we set out to scrutinize the electrical-poling effect on the $MAPbBr_3$-film-based photodetectors. Prior to the measurement, the fabricated device was connected with an external bias of 4 V (or –4 V) for poling in the dark for 5 min. The further increased poling voltage demonstrated a limited effect on further enhancing photocurrent (I_{light}). After the forward poling (i.e., the poling electric field direction is the same as the measuring electric field direction) at 4 V for 5 min in the dark, a 3.1 μA of I_{light} enhancement (from 2.1 to 5.2 μA) was obtained at 0.4 V at 27.1 mW cm^{-2} light intensity (Figure S4a, Supporting Information). Under the same measurement condition, the I_{light} was 5.4 μA after the forward poling at 10 V in the dark for 5 min, representing only 0.2 μA enhancement of the I_{light} after 6 V increasing for electrical poling. Under this condition, the poling bias voltage was set to be ±4 V for the further study. The applied bias was then set to an operating bias of 0.4 V (or –0.4 V) for photocurrent measurement. This is because the devices already showed good performance under the low measuring voltage (Figure S3d, Supporting Information). The set value of voltage is significantly lower than the poling bias voltage (±4 V), so the measuring voltage exerted little influence on the ion migration trigged by the poling in the crystals. Furthermore, the extension of poling time also yielded a limited enhancement of I_{light}. Under the same poling condition (i.e., 4 V in the dark) of forward poling, the I_{light} was increased from 2.1 to 5.2 μA for a 5 min poling (Figure S4a, Supporting Information). The I_{light} only increased to ≈6.1 μA under the same measuring condition for a long-time poling (i.e., 1 h) (Figure S4b, Supporting Information). Therefore, the poling time for this study was set to be 5 min. Moreover, an enhanced I_{light} was also observed by the forward poling when the directions of the external electric field for poling and measuring were both reversed (i.e., –4 V in the dark for poling and –0.4 V for measuring), as shown in Figure 2b. Measured at –0.4 V and under the illumination of 442 nm at a power density of 27.1 mW cm^{-2}, I_{light} was about –1.1 μA prior to the electrical poling. After poling at –4 V in the dark for 5 min, the I_{light} dramatically increased to ≈–11.0 μA, reflecting a tenfold increase over that of the device prior to poling. Although both obtained under the forward poling, the enhanced I_{light} was –9.9 μA after –4 V poling (Figure 2b) while it was only 3.1 μA after 4 V poling (Figure S4a, Supporting Information). The reason for different enhanced abilities of photocurrent under negative and positive poling biases may be attributed to the screening effect of free carriers,[35,36] which will be further discussed later. Interestingly, a reduced I_{light} was seen when the directions of electric field for measuring and poling were opposite (i.e., a reverse poling). The photocurrent was decreased from –1.1 μA (measured at –0.4 V under a 27.1 mW cm^{-2} illumination) to –0.3 μA after a reverse poling (i.e., 4 V for poling while –0.4 V for measuring) (Figure 2c). It is also interesting to note that the forward poling also caused a twofold decrease of the response time, as depicted

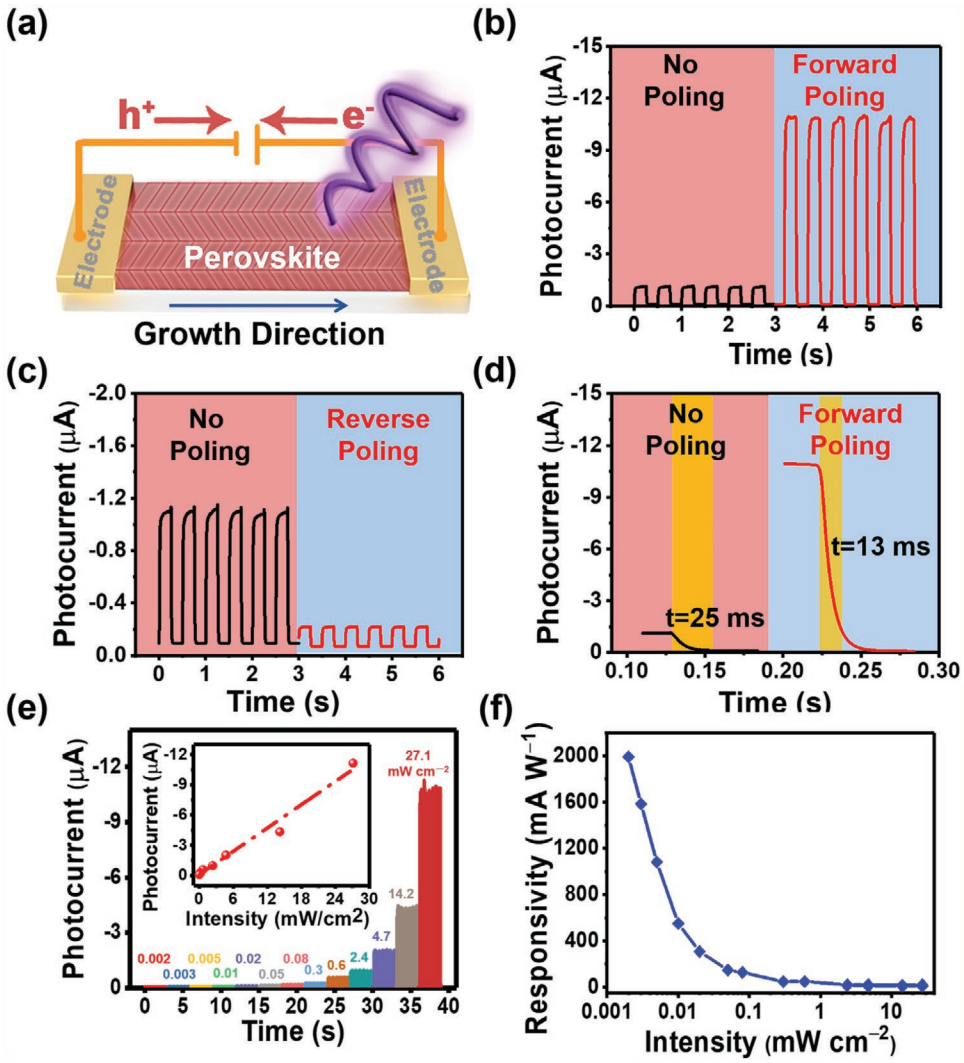

Figure 2. Device structure and optoelectronic characteristics of the $MAPbBr_3$-film-based photodetector with and without poling. a) The device architecture of a photodetector for the photoresponse measurement. b) Current–time (I–t) characteristics of the $MAPbBr_3$-film-based photodetector before (left) and after a forward poling (right) at –4 V for 5 min in the dark, measured at –0.4 V bias with a 442 nm light irradiation at a 27.1 mW cm^{-2} power intensity. c) I–t of the $MAPbBr_3$-film-based photodetector before (left) and after a reverse poling (right) at 4 V for 5 min in the dark, measured at –0.4 V bias with a 442 nm light irradiation at a 27.1 mW cm^{-2} power intensity. d) Current response of the device from switched ON to OFF before poling (left) and after a forward poling (right), showing a shorter response time of the device after poling. e) Output current of the device under different power densities of light after a forward poling at –4 V for 5 min in the dark, measured at –0.4 V bias with a 442 nm light irradiation. The inset shows the photocurrent linearity upon varying the illumination power densities after the forward poling. f) Responsivities of the device under different illumination power densities after the forward poling.

in Figure 2d. Specifically, the fall time (the time interval for the response to decay from 90% to 10% of its peak value) decreased to 13 ms after the electrical-poling process, in contrast to 25 ms of the device prior to poling. This response time is short among the $MAPbBr_3$-based photodetectors as summarized in Table S1 (Supporting Information). The tunable photocurrents together with the reduced response time signify that the underlying mechanism for the electrical-poling-induced modulation is of great significance in achieving the enhanced device performance. The typical current–time (I–t) curves of the photodetector after the forward poling under various illumination intensities are shown in Figure 2e (i.e., –4 V for poling and –0.4 V for measuring, respectively) and Figure S4c (Supporting Information) (i.e., 4 V for poling and 0.4 V for measuring), respectively. Remarkably, the device was able to detect a light intensity as weak as 2 μW cm^{-2}. Moreover, the photocurrent displayed a good linear relationship with the incident light intensity (i.e., insets in Figure 2e; Figure S4c, Supporting Information). The responsivity, R, defined as the output photocurrent, $I_{light} - I_{dark}$, divided by the incident light on the active region of a photodetector, is an important figure of merits of photodetectors to pinpoint how efficiently a photodetector responds to an optical signal. After poling, the R of the $MAPbBr_3$-film-based photodetector reached 1990 mA W^{-1} under a 2 μW cm^{-2} light intensity (Figure 2f). The large responsivity of the device is attributed mainly to the remarkable enhancement of photocurrent of

the device by electrical poling as well as the high quality of the MASP $MAPbBr_3$ film (e.g., high crystallinity and low carrier trap density). Notably, this R value is among the highest performance of $MAPbBr_3$-based photodetectors (Table S1, Supporting Information). Taken together, it is clear that after poling, the as-prepared $MAPbBr_3$-film-based photodetector exhibited a strong response to the electrical-poling process. The duration of the electrical-poling effects on the photocurrent of the $MAPbBr_3$-film-based photodetector was then examined. After stored in the dark for 1 h, the I_{light} of the polarized device (–4 V poling for 5 min in the dark) was retained at ≈ –9.8 μA (measured at –0.4 V bias with a 27.1 mW cm^{-2} power intensity) (Figure S5a, Supporting Information), an 88.3% remaining ratio of the I_{light} (–11.1 μA) after immediate poling. It is also noticed that after poling and stored in dry air for 30 days without encapsulation, the I_{light} of the device became similar to that of the device prior to poling (Figure S5b, Supporting Information), suggesting that the poling effect could be relaxed as the ions diffused back and no obvious degradation of perovskites because of the low voltage for poling and the stability of $MAPbBr_3$.[37] Due to the unique advantages of the poling process (e.g., highly efficient, easy processing, repeatable, time saving), the electrical-poling-enhanced photodetectors can be implemented for efficient and rapid detection after the calibration.

On the basis of the results above, the enhanced photocurrent and reduced response time may primarily result from the redistribution of ions in the perovskite film under electrical poling, thus modulating the optoelectronic performances (e.g., photocurrent and response time) of the device. First, it is noteworthy that as $MAPbBr_3$ at room temperature has a cubic phase, as confirmed by the XRD measurement (Figure 1f), thus, it does not meet the crystal structure for ferroelectricity, which may also contribute to the photocurrent change of perovskite-based devices under electrical poling.[38] Second, the accumulated ions would diffuse back after a period of time once all external fields are removed. This was substantiated from the experimental result that the poling effect was released after the device was stored for 30 days as the photocurrent returned to the initial level (Figure S5b, Supporting Information).

The ions redistribution would induce an internal electric field inside the optoelectronic device.[39,40] Notably, it has been reported that the ion-redistribution-triggered p–i–n junction leads to the increased open-circuit voltage and short-circuit current of solar cells.[16,25] Here, either the internal electric field or the p–i–n junction does not contribute to the enhanced photocurrents of the $MAPbBr_3$-film-based photodetector in this work due to the following two reasons. First, after the forward poling, the direction of the ion-induced internal field is opposite to the applied external electric field, which would reduce the photocurrent, contradicting the experimental results of enhanced photocurrent observed. Second, the internal electric field or the p–i–n junction induced by the ion migration would not have a strong effect over a long distance for the photodetectors due to 1 mm wide distance between two Ag electrodes and the low poling voltage. Clearly, further scrutiny is needed to understand the mechanism of ion migrations during the electrical poling on perovskite materials for the photodetector.

To examine the ion redistribution, and unravel how the ions migrate in the film and how the ion redistribution influences the metal/semiconductor junction, the surface potentials in the laterally structured photodetectors were measured before and after poling. KPFM, known as a scanning probe technique, which detects the local surface potential, was implemented to record the surface potential change of the devices. To verify the ion-migration behavior, the area that includes exclusively the pristine $MAPbBr_3$ film was first examined by KPFM, as illustrated in **Figure 3**a. After poling and reversed poling (the poling directions are indicated by the arrows in Figure 3b,c), instead of continuous color change, a clear color difference between the adjacent crystals in the KPFM images (Figure 3b,c) was found, indicating that there is a significant potential difference between crystals. This demonstrates that the ions accumulated at the interface between the crystals. Under the poling electric field, the cations and anions travel to the opposite directions within the crystals; the cations in one crystal meet anions in the other crystal; however, they are separated by the grain boundary, as illustrated in Figure S6a (Supporting Information). In this work, a low-voltage poling electric field was applied. Therefore, the ion-migration behavior in the $MAPbBr_3$-based photodetector was somewhat different from that in the reported $MAPbI_3$-based photovoltaic devices.[16,23] Under high voltage, the electric field is strong enough to trigger ions to migrate across grain boundaries and accumulate near the electrode/perovskite interface; yet in this work, the low poling voltage may not be able to impart ions to migrate across the grain boundaries. Thus, two oppositely charged ions accumulated at the interface of crystals would form the observed potential drop near the two adjacent crystals. The polarization potential of an individual crystal was rather small (≈150 mV), as revealed from the surface potential profile in Figure S6b (Supporting Information). Moreover, the $MAPbBr_3$ film crafted by MASP was composed of a number of oriented $MAPbBr_3$ crystals (1 mm wide film situated between two Ag electrodes); the poled crystals can be assumed to act like capacitors connected in series, so that a large polarization potential was produced along the direction of the electric field by accumulating the capacitance in the $MAPbBr_3$ layer between the electrodes. Remarkably, the different surface potential distribution among crystals was able to be reversed in the perovskite layer by altering the direction of electric field for poling. After poling, three parallel regions with gradually lightened color along the direction of electric field were presented in the surface potential image (Figure 3b). After reversed poling, the cations and anions redistribute to the opposite directions within the crystals, as displayed in Figure S6c (Supporting Information). These parallel areas became progressively darkened in the KPFM image (Figure 3c). These observations further substantiate that ion migration within crystals is induced by the poling process.

Due to the fact that ion migration only occurs in the perovskite layer, the area that includes both one electrode (as a reference) and $MAPbBr_3$ was examined by KPFM, as illustrated in Figure 3d. For the device prior to poling, the area of $MAPbBr_3$ in the KPFM image showed a higher surface potential than that of Ag electrode due to their different work functions (Figure 3e). After poling (the poling direction is indicated by the arrow), the difference of surface potentials of Ag and $MAPbBr_3$ became smaller (Figure 3f), signifying that the polarization was induced in the perovskite layer due to the ion migration. The surface

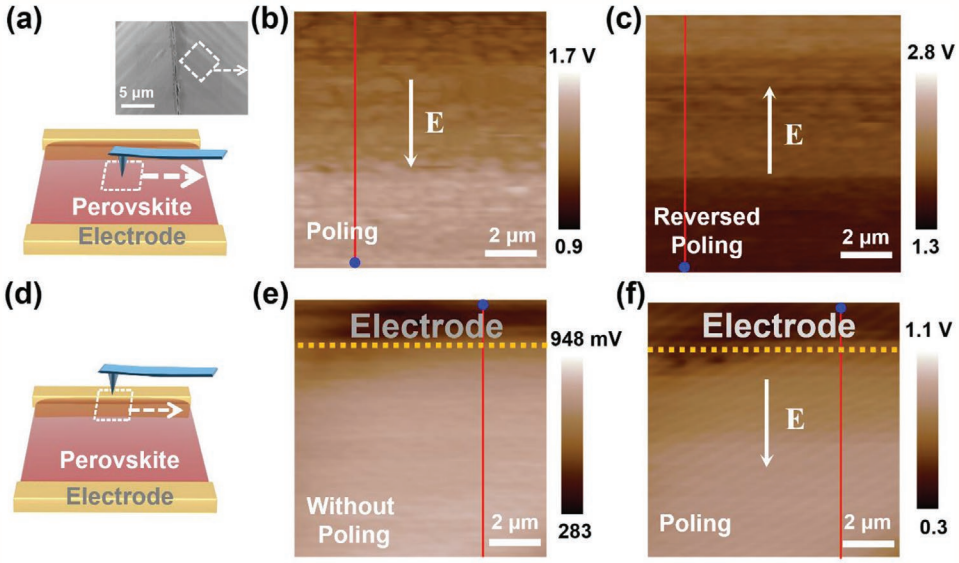

Figure 3. Kelvin probe force microscopy (KPFM) measurements on the $MAPbBr_3$-film-based photodetector with and without poling. a) Schematic illustration of the KPFM measurement exclusively in the $MAPbBr_3$ area. The white dashed box represents the scanning region. b,c) KPFM potential images of $MAPbBr_3$-film-based device in the $MAPbBr_3$-only area after a forward poling at 4 V for 5 min in the dark (b), and after a reversed poling at –4 V for 5 min in the dark (c). d) Schematic illustration of the KPFM measurement in the perovskite/electrode ($MAPbBr_3$/Ag) area. The white dashed box indicates the scanning region. e,f) KPFM surface potential images of the $MAPbBr_3$-film-based photodetector taken in the $MAPbBr_3$/Ag area before electrical poling (e) and after electrical poling at 4 V for 5 min in the dark (f). The white arrows in (b), (c), and (f) reflect the direction of the applied electric field for poling. The red lines in (b), (c), (e), and (f) show the scan position of the surface potential profiles as in Figures S6 and S7 (Supporting Information), respectively, with the blue dots at the end of lines marking the starting points. The bias voltage applied to the tip of KPFM was 3 V for all the measurements.

potential difference between Ag and $MAPbBr_3$ before and after poling was reduced from ≈240 mV before poling to ≈120 mV after poling (Figure S7a and Figure S7b, respectively, in the Supporting Information). Consequently, ion redistribution was able to modulate the junction in the $MAPbBr_3$-film-based photodetector by electrical poling, and ion-redistribution-induced polarization potential was, in turn, capable of modulating the device performance.

In stark contrast, the $MAPbBr_3$-stripe-based photodetector displayed a negligible photocurrent change before and after forward poling. As shown in Figure S8a (Supporting Information), the I_{light} of a stripe-based photodetector was roughly –0.4 μA prior to poling (measuring at –0.4 V, under 442 nm light illumination with a power intensity of 27.1 mW cm^{-2}), displaying only a little difference with the I_{light} of a film-based photodetector (–1.1 μA). However, the I_{light} of the stripe-based photodetector was retained at ≈–0.4 μA after the forward poling under the same measuring condition as that prior to poling (Figure S8b, Supporting Information). Although the two forms of perovskite layers (i.e., film and stripes) were crafted by the MASP technique using the same precursors, the electrical-poling process showed the greatly different impacts on the corresponding photodetectors. Thus, our study represents the first investigation into the forms of perovskite layers that influence the electrical-poling process on the resulting performance of hybrid perovskite-based devices.

To clarify the mechanism for the different effects of electrical poling on film-based and stripe-based photodetectors, the stripe-based photodetector also examined by KPFM. An insignificant change of surface potential among crystals was observed in the $MAPbBr_3$-stripe-based photodetector after electrical poling (Figure S9a,c, Supporting Information) and the subsequently reversed poling (Figure S9b,d, Supporting Information), as revealed by the surface potential images (Figure S9a,b, Supporting Information) and the surface potential profiles (Figure S9c,d, Supporting Information), respectively. Clearly, no polarization potential was generated among crystals in the stripe-based device during the electrical poling. This result is correlated well with the negligible enhancement of photocurrent in the stripe-based photodetector after the forward poling (Figure S8, Supporting Information). In film-based device, the crystals are closely packed one after another (Figure 1d), so that each small polarization potential of an individual crystal can be added up to a large potential. For the stripe-form photodetector, the larger gaps between crystals (Figure S2b, Supporting Information) hinder the adding-up of the poled crystals, so a large polarization potential among the crystals will not be created to modulate the photocurrent of the stripe-form photodetector. Such different ion-migration behaviors under electrical poling are regarded as the origin that accounts for the different poling effects on the film-form and stripe-form photodetectors.

Figure 4 illustrates the photocurrent modulation in the perovskite-film-based photodetector under electrical poling. The device shows a Schottky junction behavior under illumination (*I–V* curves in Figure S3a,b, Supporting Information), as noted above, because the photoexcited carriers in the photodetector had preferential directionality for transport. In the absence of electrical poling, the band diagram of the device under bias (measuring condition) is displayed in Figure 4a. The Fermi levels of $MAPbBr_3$ and Ag electrode in this diagram

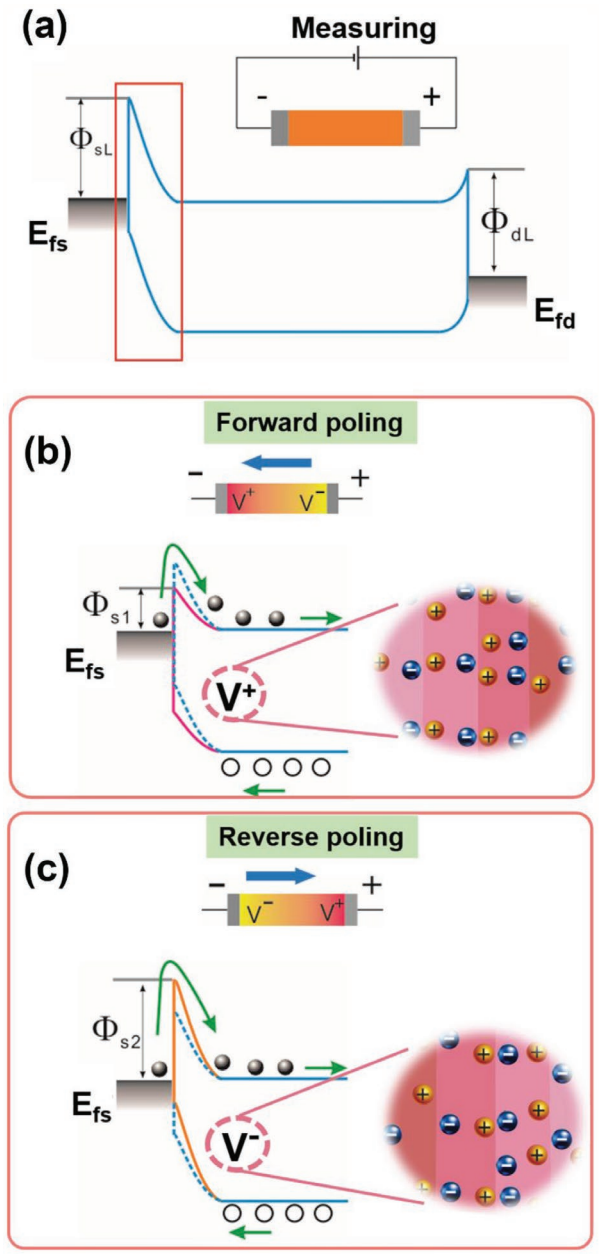

Figure 4. Proposed mechanism for the photocurrent modulation in the perovskite-film-based photodetector under electrical poling. Schematic illustration of band diagrams of the $MAPbBr_3$-film-based photodetector during the photocurrent measurement a) without poling, b) after a forward poling, and c) after a reverse poling. The insets in (b) and (c) depict the ions' redistribution in $MAPbBr_3$ crystals after the forward and the reverse poling, respectively. The blue curves are the energy bands at the initial stage with no poling, and the pink and yellow curves in (b) and (c) are the energy bands after the forward and the reverse poling, respectively. The schematic illustration of circuit in (a) shows the measuring condition for the photodetector. The symbols of "+" and "–" represent the electric field direction of the applied bias for measuring the photocurrent. The red rectangle in (a) indicates the position of (b) and (c). The straight thick blue arrows in (b) and (c) mark the direction of the external electric field for poling. The devices below the blue arrows illustrate the polarization potential within perovskite layer after poling. The curved arrows in (b) and (c) refer to the electron injection from Ag electrode to $MAPbBr_3$.

shift due to the applied bias for measuring the photodetector. In the back-to-back contacts, Schottky barrier height (SBH) at the drain and source sides would be created between the perovskite and the Ag electrode. The SBH at the source side is the main part for consideration when a positive voltage was applied at the drain side, because the voltage drop occurred primarily at the reversely biased Schottky barrier at the source side. Therefore, the change of the SBH at the source side and its effect on photocurrent will be further discussed after electrical poling, as displayed in Figure 4b,c. In addition, when the device is under illumination, the incident photons give rise to electron–hole pairs in the perovskite. Under an external electric field, the photogenerated electrons in the conductive band are inclined to move close to the drain side, and the holes in the valence band tend to move toward the source side. Typically, the photocurrent depends on the effective separation and transport of both holes and electrons in the vicinity of the contacts, and strongly affects the SBH as a result of the thermionic field emission (TFE) theory.[41] During the forward poling, the cations (i.e., MA^+ and Pb^{2+}) in the $MAPbBr_3$ film move along the direction of the applied electric field (blue thick arrow in Figure 4b) while the anions (i.e., Br^-) travel to the opposite direction of the electric field inside crystals. After poling, an ion redistribution is achieved within $MAPbBr_3$ crystals, as demonstrated in the inset of Figure 4b. As discussed above, a large positive polarization potential is yielded in the $MAPbBr_3$ film toward the source side due to the accumulated cations within the $MAPbBr_3$ crystals at the microscale (Figure 4b). Similar to the polarization caused by piezoelectric,[42] the polarization potential could be created by ion migration via poling. Such a polarization potential modulates the photocurrents of optoelectronic devices, by modifying the concentration and distribution of free carriers in perovskite in the vicinity of the Schottky barrier.[43] Generally, this ion-migration-induced positive polarization potential lowers the SBH ($\Phi_{s1} < \Phi_{sL}$) after the electrical poling,[42] which could facilitate the injection of electrons into the $MAPbBr_3$ film, thereby resulting in a significantly enhanced photocurrent and reduced response time. Conversely, during the reverse poling, a large negative polarization potential is induced toward the source side owing to the accumulated anions (inset in Figure 4c), thus leading to an enlarged SBH ($\Phi_{s2} > \Phi_{sL}$, Figure 4c). The higher barrier repels the electrons near the metal–semiconductor interface and contributes to the decrease of photocurrent. Therefore, the polarization potential modulates the barrier height at the perovskite/electrode interface (i.e., the interfacial modulation), which, in turn, regulates the photocurrent (i.e., tunable photocurrents; Figure 4b,c). It is important to note that such a photocurrent tailoring can be conveniently performed after the fabrication of devices by capitalizing on the electrical poling.

We also investigated the change of photoresponse by reversing both directions of poling and measuring biases. It was found that the enhancement of photocurrent obtained from –4 V poling and –0.4 V measurement (Figure 2b) was –9.9 A while that yielded from 4 V poling and 0.4 V measurement was only 3.1 A (Figure S4a, Supporting Information). Under the positive bias voltage for poling, it has a smaller enhanced photocurrent. This is attributed to the fact that, under positive voltage, there are a larger amount of free carriers

due to the larger current (Figure S3a, Supporting Information), which would screen the polarization potential[35,36] and thus make the modulation of the polarization potential weak. This observation also highlights the significant role of polarization potential for tuning photocurrents of the $MAPbBr_3$-film-based photodetectors.

In summary, we demonstrated that the electrical poling could significantly promote the optoelectronic process in hybrid perovskite photodetectors, thereby attaining high photocurrent and responsivity as well as fast response time. By capitalizing on the MASP technique, the forms of perovskite layers with either oriented, continuous film or separated stripes can be readily accessed, thereby enabling the investigation into the electrical-poling effect using a low voltage (0.004 V μm^{-1}) on the photodetectors of different morphologies. The KPFM study reveals that, under the applied bias, the ion redistribution within the perovskite crystal grains induces the polarization potential in oriented, continuously grown perovskite crystals. The accumulation of local polarization potential in the vicinity of the junction during the electrical poling at the microscale is viewed to be responsible for the tunable photocurrents in the perovskite-film-based photodetector. This work may provide a unique platform for developing a variety of high-performance optoelectronic devices by implementing a diversity of perovskite materials of interest via judiciously exploiting electrical-poling-induced ion migrations and thus polarization potential in perovskites.

Experimental Section

MASP of Perovskite Layer: For producing the $MAPbBr_3$ film, the precursor solution was prepared by dissolving 11.3 mg of MABr and 38.7 mg of $PbBr_2$ in 1 mL DMF, and then stirred at 60 °C for 1 h to form a 50 mg mL^{-1} $MAPbBr_3$ precursor DMF solution. About 20 µL of the solution was injected and confined between two nearly parallel plates (i.e., a movable flat lower substrate and a stationary slightly titled upper blade) because of the capillary effect. The separation distance between these two plates was ≈200 µm. It was notable that the lower substrate was pretreated by oxygen plasma for 15 min. The lower substrate was ≈1.5 cm × 1.5 cm and the upper blade was ≈2.0 cm × 1.4 cm. The motion of the lower substrate was controlled by a computer-programmed translational stage (Parker Hannifin Corp, Mode MX80LVixBL2b). The moving speed of the lower substrate was 25 µm s^{-1} in the direction opposite to the receding meniscus. During the MASP process, the lower substrate was heated at 100 °C by a temperature-controlled microscope stage (Linkam TMS 94 LTS 350). A continuous $MAPbBr_3$ film was yielded after the complete evaporation of the precursor solution. Further annealing was conducted on the as-obtained perovskite film at 100 °C for 5 min. The MASP process of $MAPbBr_3$ stripes was similar to that of $MAPbBr_3$ film except that the concentration of the precursor DMF solution was 10 mg mL^{-1}.

Fabrication of Photodetectors: The MASP-enabled perovskite layer on a glass substrate was fixed in a mask. Then, two silver (Ag) electrodes with 200 nm thickness were thermally deposited on the perovskite layer, yielding the photodetector. The lateral distance between the two Ag electrodes was 1 mm.

Electrical Poling on Photodetectors: The electrical-poling process was performed on photodetectors in the dark for a period of time (e.g., 5 min, 1 h) before measurement. The applied voltage for poling on devices was supplied by a Stanford Research DS345 Synthesized Function Generator through two electrodes on perovskite film. After poling in the dark, the photoelectric properties (e.g., photocurrent and response time) were measured immediately under 442 nm visible light illumination at a certain power density and an applied bias voltage to evaluate the poling effects on perovskite-based photodetectors.

Characterizations: The morphologies of perovskite layers were acquired by a Hitachi SU8010 SEM. The XRD measurement was performed using a PANalytical X'Pert PRO X-ray diffractometer. The UV–vis spectrum was recorded using a Shimadzu UV-2600 spectrophotometer with a photometric integrating sphere. The photoluminescence spectrum was obtained by a PerkinElmer LS 55 PL spectrophotometer. The *I–V* characteristics of photodetectors were measured by a computer-controlled measurement system with a Stanford SRS low-noise current preamplifier (SR570)/SRS low-noise voltage preamplifier (SR560) in conjunction with a General-Purpose Interface Bus (GPIB) controller (GPIB-USB-HS, NI 488.2). The 442 nm optical input stimuli were provided by a He–Cd laser (model no. KI5751I-G, Kimmon Koha Co., Ltd.). The power densities of light were measured by a power meter (Newport 1919-R). The surface potentials of the devices were detected by atomic force microscopy (AFM, MFP-3D, Asylum Research) in a KPFM mode. The KPFM was measured under an amplitude mode.

Supporting Information

Supporting Information is available from the Wiley Online Library or from the author.

Acknowledgements

C.L. and H.Z. contributed equally to this work. This work was supported by the NSF (ECCS 1914562 and CMMI 1727313). C.L. gratefully acknowledges the financial support from the China Scholarship Council.

Conflict of Interest

The authors declare no conflict of interest.

Keywords

electrical poling, hybrid perovskites, ion migration, photodetectors, polarization potential

Received: August 12, 2020
Revised: September 23, 2020
Published online:

[1] M. He, B. Li, X. Cui, B. Jiang, Y. He, Y. Chen, D. O'Neil, P. Szymanski, M. Ei-Sayed, J. Huang, Z. Lin, *Nat. Commun.* **2017**, *8*, 16045.
[2] B. Chen, X. Zheng, Y. Bai, N. Padture, J. Huang, *Adv. Energy Mater.* **2017**, *7*, 1602400.
[3] Y. Yoon, Y. Chang, S. Zhang, M. Zhang, S. Pan, Y. He, C. Lin, S. Yu, Y. Chen, Z. Wang, Y. Ding, J. Jung, N. Thadhani, V. Tsurkruk, Z. Kang, Z. Lin, *Adv. Mater.* **2019**, *31*, 1901602.
[4] J. Huang, Y. Yuan, Y. Shao, Y. Yan, *Nat. Rev. Mater.* **2017**, *2*, 17042.
[5] N. Jeon, J. Noh, Y. Kim, W. Yang, S. Ryu, S. Seok, *Nat. Mater.* **2014**, *13*, 897.
[6] M. Zhang, X. Cui, Y. Wang, B. Wang, M. Ye, W. Wang, C. Ma, Z. Lin, *Nano Energy* **2020**, *71*, 104620.
[7] Y. Kim, H. Cho, T. Lee, *Proc. Natl. Acad. Sci. USA* **2016**, *113*, 11694.

[8] S. Cho, M. Park, Y. Kim, C. Wolf, C. Lee, J. Heo, A. Sadhanala, N. Myoung, S. Yoo, S. Im, R. Friend, T. Lee, *Science* **2015**, *350*, 1222.
[9] S. Senanayak, B. Yang, T. Thomas, N. Giesbrecht, W. Huang, E. Gann, B. Nair, K. Goedel, S. Guha, X. Moya, C. McNeill, P. Docampo, A. Sadhanala, R. Friend, H. Sirringhaus, *Sci. Adv.* **2017**, *3*, e1601935.
[10] J. Zhou, J. Huang, *Adv. Sci.* **2018**, *5*, 1700256.
[11] H. Wang, D. Kim, *Chem. Soc. Rev.* **2017**, *46*, 5204.
[12] M. He, D. Zheng, M. Wang, C. Lin, Z. Lin, *J. Mater. Chem. A* **2014**, *2*, 5994.
[13] T. Brenner, D. Egger, L. Kronik, G. Hodes, D. Cahen, *Nat. Rev. Mater.* **2016**, *1*, 15007.
[14] N. Vicente, G. Belmonte, *Adv. Energy Mater.* **2017**, *7*, 1700710.
[15] M. Bastiani, G. Dell'Erba, M. Gandini, V. D'Innocenzo, S. Neutzner, A. Kandada, G. Grancini, M. Binda, M. Prato, J. Ball, M. Caironi, A. Petrozza, *Adv. Energy Mater.* **2016**, *6*, 1501453.
[16] Y. Yuan, J. Chae, Y. Shao, Q. Wang, Z. Xiao, A. Centrone, J. Huang, *Adv. Energy Mater.* **2015**, *5*, 1500615.
[17] G. Xia, B. Huang, Y. Zhang, X. Zhao, C. Wang, C. Jia, J. Zhao, W. Chen, J. Li, *Adv. Mater.* **2019**, *31*, 1902870.
[18] E. Hoke, D. Slotcavage, E. Dohner, A. Bowring, H. Karunadasa, M. McGehee, *Chem. Sci.* **2015**, *6*, 613.
[19] X. Chin, D. Cortecchia, J. Yin, A. Bruno, C. Soci, *Nat. Commun.* **2015**, *6*, 7383.
[20] Y. Yuan, J. Huang, *Acc. Chem. Res.* **2016**, *49*, 286.
[21] A. Bruno, D. Cortecchia, X. Chin, K. Fu, P. Boix, S. Mhaisalkar, C. Soci, *Adv. Energy Mater.* **2017**, *7*, 1700265.
[22] Y. Kim, N. Jeon, J. Noh, W. Yang, J. Seo, J. Yun, A. Ho-Baillie, S. Huang, M. Green, J. Seidel, T. Ahn, S. Seok, *Adv. Energy Mater.* **2016**, *6*, 1502104.
[23] Z. Xiao, Y. Yuan, Y. Shao, Q. Wang, Q. Dong, C. Bi, P. Sharma, A. Gruverman, J. Huang, *Nat. Mater.* **2015**, *14*, 193.
[24] D. Moia, I. Gelmetti, P. Calado, W. Fisher, M. Stringer, O. Game, Y. Hu, P. Docampo, D. Lidzey, E. Palomares, J. Nelson, P. Barnes, *Energy Environ. Sci.* **2019**, *12*, 1296.
[25] Y. Yuan, T. Li, Q. Wang, J. Xing, A. Gruverman, J. Huang, *Sci. Adv.* **2017**, *3*, e1602164.
[26] Y. Zou, R. Holmes, *Adv. Energy Mater.* **2016**, *6*, 1501994.
[27] P. Wangyang, C. Gong, G. Rao, K. Hu, X. Wang, C. Yan, L. Dai, C. Wu, J. Xiong, *Adv. Opt. Mater.* **2018**, *6*, 1701302.
[28] J. Lee, D. Lee, D. Jeong, N. Park, *Adv. Funct. Mater.* **2019**, *29*, 1807047.
[29] W. Han, Z. Lin, *Angew. Chem., Int. Ed.* **2012**, *51*, 1534.
[30] Y. Chen, Q. Ge, Y. Shi, J. Liu, D. Xue, J. Ma, J. Ding, H. Yan, J. Hu, L. Wan, *J. Am. Chem. Soc.* **2016**, *138*, 16196.
[31] Y. Liu, Z. Yang, D. Cui, X. Ren, J. Sun, X. Liu, J. Zhang, Q. Wei, H. Fan, F. Yu, *Adv. Mater.* **2015**, *27*, 5176.
[32] H. Zhu, Y. Fu, F. Meng, X. Wu, Z. Gong, Q. Ding, M. Gustafsson, M. Trinh, S. Jin, X. Zhu, *Nat. Mater.* **2015**, *14*, 636.
[33] M. Saidaminov, V. Adinolfi, R. Comin, A. Abdelhady, W. Peng, I. Dursun, M. Yuan, S. Hoogand, E. Sargent, O. Bakr, *Nat. Commun.* **2015**, *6*, 8724.
[34] Effect of beam size on photodiode saturation. https://www.thorlabs.com/images/TabImages/Beam_Size_and_photodiode_Saturation_LabFact.pdf (accessed June 2020).
[35] H. Zou, X. Li, G. Dai, W. Peng, Y. Ding, Y. Zhang, A. Wang, S. Zhang, C. Xu, S. Zhang, Z. Wang, *ACS Nano* **2019**, *13*, 12259.
[36] W. Wu, L. Wang, R. Yu, Y. Liu, S. Wei, J. Hone, Z. Wang, *Adv. Mater.* **2016**, *28*, 8463.
[37] X. Zheng, B. Chen, M. Yang, C. Wu, B. Orler, R. Moore, K. Zhu, S. Priya, *ACS Energy Lett.* **2016**, *1*, 424.
[38] S. Wang, X. Liu, L. Li, C. Ji, Z. Sun, Z. Wu, M. Hong, J. Luo, *J. Am. Chem. Soc.* **2019**, *141*, 7693.
[39] R. Saraf, L. Pu, V. Maheshwari, *Adv. Mater.* **2018**, *30*, 1705778.
[40] H. Wang, M. Zhou, H. Luo, *ACS Omega* **2018**, *3*, 1445.
[41] F. Padovani, R. Stratton, *Solid-State Electron.* **1966**, *9*, 695.
[42] W. Wu, L. Wang, Y. Li, F. Zhang, L. Lin, S. Niu, D. Chenet, X. Zhang, Y. Hao, T. Heinz, J. Hone, Z. Wang, *Nature* **2014**, *514*, 470.
[43] H. Zou, X. Li, W. Peng, W. Wu, R. Yu, C. Wu, W. Ding, F. Hu, R. Liu, Y. Zi, Z. Wang, *Adv. Mater.* **2017**, *29*, 1701412.